ISSN 1063-7710, Acoustical Physics, 2016, Vol. 62, No. 2, pp. 169–178. © Pleiades Publishing, Ltd., 2016.
Original Russian Text © E.A. Annenkova, S.A. Tsysar', O.A. Sapozhnikov, 2016, published in Akusticheskii Zhurnal, 2016, Vol. 62, No. 2, pp. 167–177.

PHYSICAL ACOUSTICS

Constructing Ultrasonic Images of Soft Spherical Scatterers

E. A. Annenkova[a], S. A. Tsysar'[a], and O. A. Sapozhnikov[a, b]

[a] *Moscow State University, Moscow, 119991 Russia*
e-mail: a-a-annenkova@yandex.ru
[b] *Center for Industrial and Medical Ultrasound, Applied Physics Laboratory, University of Washington, Seattle, WA 98105, USA*
Received March 25, 2015

Abstract—The paper considers specific features of ultrasonic visualization of gas bubbles in a liquid or a medium of like soft biological tissue type under conditions when the size of scatterers is comparable to the acoustic wavelength. It was proposed to use styrofoam specimens as the experimental model of stationary gas bubbles. Patterns of ultrasound scattering by a styrofoam sphere in water were obtained experimentally. It was shown that the measurement results agree well with the prediction of the classical theoretical model of scattering of a plane wave by a perfectly soft sphere. Several experiments were performed illustrating the specific features of visualizing millimeter-sized bubbles. A Terason commercial ultrasonic scanner was used; gelatin specimens with embedded styrofoam spheres served as the objects of study. The simulation and experimental results showed that when bubbles with diameters of <1 mm are visualized, it is impossible to measure the diameter of scatterers because bubbles of different diameters are imaged as bright spots of identical diameter, which is equal to the scanner resolution. To eliminate this difficulty, it is recommended to use the results of theoretical simulation performed in this study, which revealed a monotonic increase in the backscattered signal intensity with an increase in bubble radius. An ultrasonic visualization mode is proposed in which the brightness of scattered signals is used to differentiate between bubbles of different size.

Keywords: ultrasonic diagnostics, scattering, millimeter-sized gas bubbles

DOI: 10.1134/S1063771016020020

1. INTRODUCTION

Ultrasonic visualization is actively used in nondestructive testing and medicine [1, 2]. Image construction is based on analysis of echo pulses that arise when short probing pulses are scattered by inhomogeneities of the medium. In medical diagnostics, ultrasound propagates in weakly inhomogeneous soft biological tissues, in which scattering is rather weak; therefore, the image construction is based on weak scattered signals. High-intensity signals are artificially restricted when processing scattering data. As a result, scatterers of different strengths may have identical images (in the form of bright regions).

There are diagnostic situations in which it is important to visualize and differentiate both weak and strong scatterers. An example of such objects is vapor–gas bubbles of different sizes, from microns to millimeters, which arise in a biological tissue during therapy using high-intensity focused ultrasound. When the acoustic cavitation threshold is exceeded, gas bubbles with dimensions that range from several microns to several tens of microns arise in the medium, and if ultrasound heats the tissue up to boiling, larger vapor–gas bubbles appear that may grow and reach diameters of several millimeters [3, 4]. Both small cavitation bubbles and large bubbles that appear during tissue boiling are strong scatterers; therefore, they are displayed in an ultrasonic image in the B mode as bright spots with a size that exceeds the scanner resolution. As a rule, the form of these spots gives no definite information on the bubble size; thus, it is difficult to determine the phenomenon, either the cavitation or boiling, that occurred in the tissue in the region of therapeutic action. Depending on the bubble size and features of the bubble dynamics in an acoustic field, various biological effects arise; therefore, the ability to distinguish between bubbles of different sizes using ultrasonic images thereof is of practical significance.

Note that micron-sized cavitation bubbles can scatter ultrasound in the resonant manner [5, 6], but larger bubbles that are produced during boiling behave more likely as stationary empty cavities for megahertz-frequency waves in water. In order to reveal the dependence of a backscattering signal on the bubble size, it is necessary to simulate the process of ultrasonic pulses being scattered by a stationary empty cavity. Numerical simulation of this process can use the known theoretical model of scattering of a plane acoustic wave by a perfectly soft sphere [7]. This model is an important example of exactly solved diffraction problems.

There are a few studies devoted to diagnostics of strongly scattering objects with dimensions on the order of the instrument resolution or even smaller, despite the fact that such objects may appear in certain

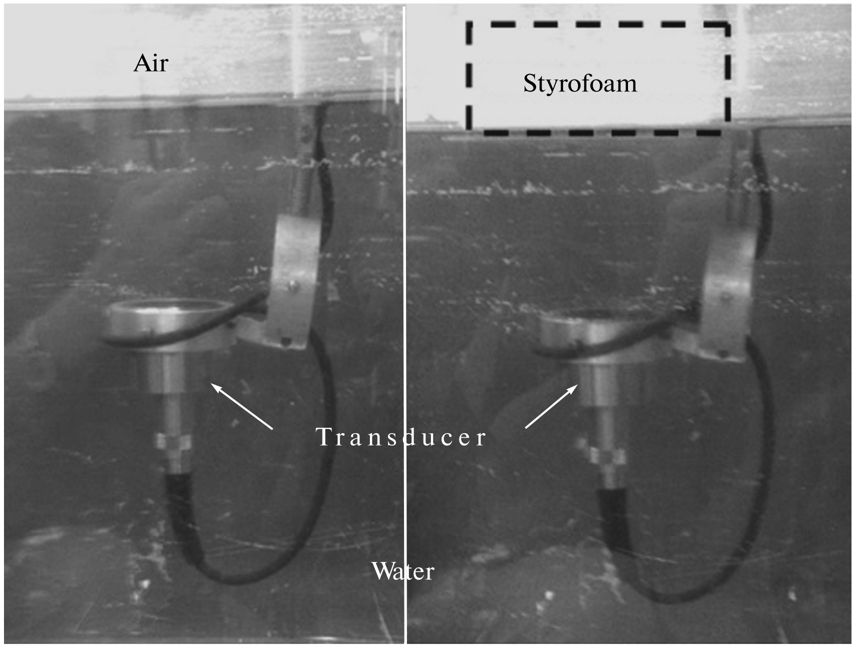

Fig. 1. Experiment on comparing coefficients of wave reflection from flat air–styrofoam interfaces.

situations in the bodies of human beings or animals and influence biological processes. Therefore, acoustic microscopy studies are noteworthy, in which images are obtained by scanning the investigated region with a high-frequency single-element transducer, which is coupled to an acoustic lens. Some aspects of the formation of images of spherical scatterers were considered in a number of studies in this field [8, 9]. Similar, although not identical problems arise when visualizing bubbles using the multielement transducers of medical diagnostic scanners. This study refers just to this field of investigation.

2. EXPERIMENTAL STUDY OF REFLECTION FROM A FLAT INTERFACE

An experimental study of ultrasound scattering by a millimeter-sized gas bubble under ordinary conditions is rather difficult, since a bubble reaches the surface very quickly under the action of the buoyancy force, and the use of holding accessories inevitably distorts the spherical shape of the scatterer. Therefore, when investigating scattering, it is desirable to replace a gas bubble with a sphere of a mechanically stiff but acoustically soft (in comparison to water) material. Styrofoam with a density much lower than the water density is one such material. To test the possibility of using styrofoam as the material for the acoustic model of a gas medium, a number of experiments on comparing the reflection properties of styrofoam and air were carried out. The goal was to verify whether the acoustic-wave reflection coefficient for styrofoam in water is indeed close to the coefficient of reflection from air and this value is close to -1. In a general case, the coefficient of reflection from such media may differ from this value [10].

The schematic of the first experiment is illustrated by photographs in Fig. 1. A flat ultrasonic transducer with a diameter of 38 mm (Model V392-SU, Olympus, Waltham, MA, USA) was oriented so that its normal was directed vertically upward. It was placed in a bath with degassed water at a distance of 5.5 cm from the free water–air interface. The transducer was excited with a high-frequency voltage from a signal generator (Model 33120A, Agilent Technologies Inc., Santa Clara, CA). The voltage at the transducer was recorded with an oscilloscope (Tektronix 520A, Beaverton, Oregon, USA). A pulse consisting of 20 cycles was radiated at a frequency of 1 MHz, and a surface-reflected echo signal was recorded.

The flat side of a styrofoam block was then placed horizontally on the water surface with an immersion depth of 1–2 mm, and a styrofoam-reflected pulse was recorded in a similar way (Fig. 1). The cross-sectional size of the reflecting surface (~10 cm) was much larger than the ultrasonic beam diameter (~4 cm). Note that in order to avoid the formation of an air layer between styrofoam and water, the styrofoam block was initially fully submerged in water and turned so that the reflecting side could be vertical for some time. This surface was then wiped to remove bubbles that stuck to it, and only after this was the reflecting surface finally positioned horizontally. The typical result of observations is shown in Fig. 2. The virtually complete coincidence of both the amplitudes and phases of two reflected pulses indicates that the coefficients of reflection from

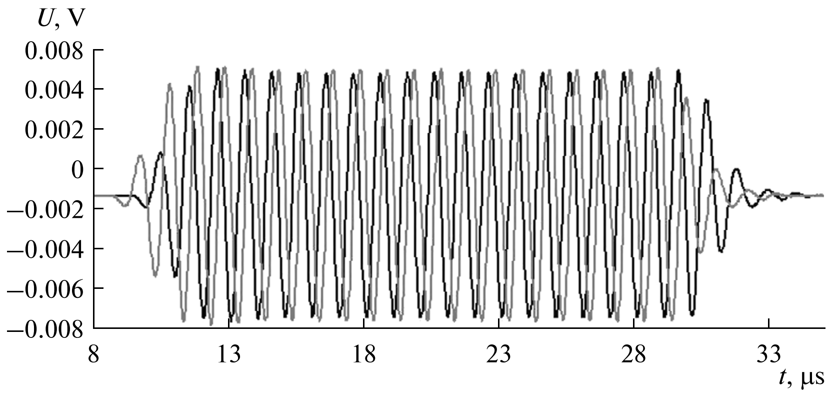

Fig. 2. Acoustic pulses reflected from water–air (black line) and water–styrofoam (gray line) interfaces. A certain advance of signal arrival from styrofoam (~0.5 μs) is explained by slight immersion of the reflecting surface relative to the initial water level.

the water–air and water–styrofoam interfaces are close to each other and that styrofoam actually behaves as an acoustically soft material.

The fact that the reflected signal is averaged over the transducer surface can be regarded as a certain drawback to the described experiment. In order to lift this restriction, we performed another experiment, in which the measured signals were not spatially averaged. The measurements were performed with the same transducer used as the ultrasound source, but the reflected signal was received with a separate hydrophone. The normal to the source had a horizontal direction. Just like in the above-described experiment, measurements were performed in two stages, with the styrofoam block and without it, but other characteristics were compared, namely, the 2D wave amplitude and phase distributions in the reflected and freely propagating beams at the same distance from the source.

When studying the acoustic properties of styrofoam the plane reflecting surface was set at an angle of 45° to the direction of the incident beam so that the reflected beam continued to propagate in the horizontal direction normally to the initial incident beam. The 2D transverse wave amplitude and phase distributions were measured in the vertical plane, which was perpendicular to the reflected beam axis, beyond the zone of the incident beam. Measurements were performed with a hydrophone with a sensitive area of 0.15 mm in diameter (Model GL-0150, SEA, CA, USA). Note that the ultrasound wavelength at the operating frequency was 1.5 mm; i.e., the sensor could be considered a point sensor. The hydrophone was installed on a computer-controlled micropositioning system (Velmex Inc., Bloomfield, NY, USA), which allowed the field to be spatially scanned with an accuracy of up to 2.5 μm. The scanning pitch was 0.5 mm. After these measurements of the reflected beam parameters, the styrofoam block was taken out of the water and the hydrophone was oriented toward the source and placed at such a distance from it that the front delay of the received signal on the beam axis coincided with the delay recorded for the styrofoam-reflected signal in the first part of the experiment. Subsequently, the field was scanned again in the transverse plane; thus, the 2D wave amplitude and phase distributions for the freely propagating beam were determined.

The measurement results are shown in Fig. 3. The phase distributions of the considered fields show that the scanning plane was positioned along the wave front of the beam with a high accuracy (the phase gradient is small, about 1 rad/cm); thus, both scanning surfaces were virtually perpendicular to the beam axis. The cross-sectional amplitude distribution in the freely propagating beam has a smooth circular structure. This structure is slightly distorted in a reflected beam, which can be explained by the presence of small irregularities on the styrofoam surface. This distortion does not allow comparison of the local field values in two cases. At the same time, it is possible to compare the powers of the incident and reflected beams. For this purpose, the total power was calculated with an accuracy to within the same factor, which is determined by the hydrophone sensitivity, for each of the measured amplitude distributions. Because the measured transverse phase change was found to be small in both cases, the power could be considered proportional to the integral of the amplitude squared. As a result of this calculation, the reflected beam power was found to be approximately 91% of the incident beam power. This value is close to 100%; i.e., styrofoam indeed reflects as an acoustically soft material. A slight decrease in the total power of the reflected beam can be due to the fact that a part of the reflected signal did not reach the scanned area because of surface irregularities on the styrofoam plate (this is seen in the lower part of the reflected-signal amplitude distribution in Fig. 3).

3. SCATTERING BY SPHERICAL SPECIMENS

3.1. Experiment

Since the above-described experiment with an extended flat FM specimen confirmed that styrofoam

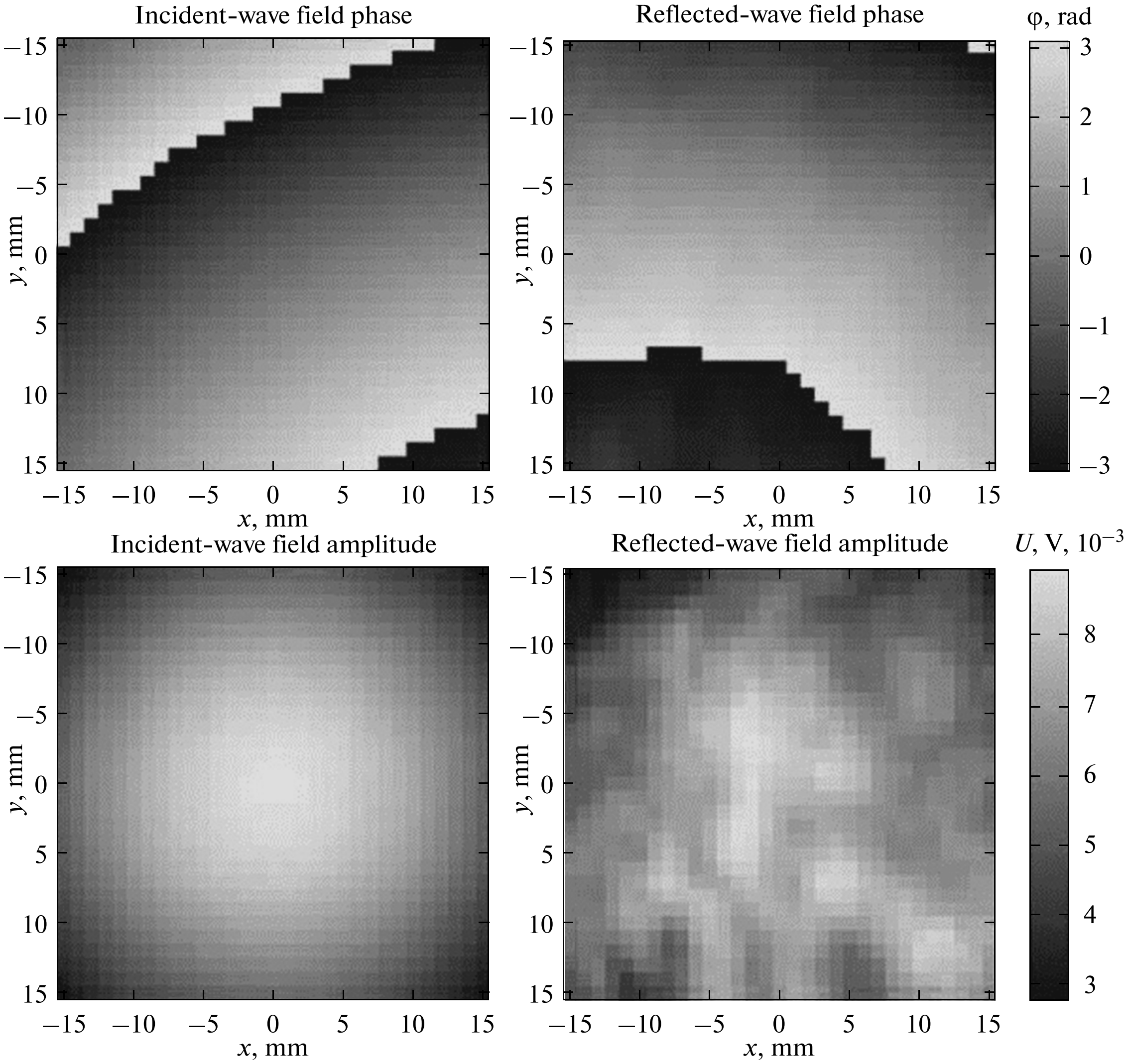

Fig. 3. Distributions of phase and amplitude of fields of incident and styrofoam-reflected waves.

is close to air in its acoustic properties, it can be expected that small spherical styrofoam specimens will scatter ultrasound as empty cavities. This was checked with a number of experiments on obtaining the scattering patterns for a soft-sphere model. A styrofoam ball with a 5-mm radius was taken as the model. It was fixed in a rigid frame on an acoustically transparent thin filament (a 50 μm-diameter nylon fishing line) with an adhesive so that it would not come to the surface when immersed in water (Fig. 4).

The experimental setup consisted of the same elements (a generator, an ultrasonic transducer, an oscilloscope, a hydrophone, and a micropositioning system) as those in the above-described experiments. Measurements were performed in the following order. First, in the presence of a spherical scatterer, raster scanning of the transverse ultrasonic field structure was performed in the region behind it. The signal amplitude A_{total} and phase φ_{total} were measured at each point; i.e., the cross-sectional distribution of the complex amplitude $P_{\text{total}} = A_{\text{total}} \exp(i\varphi_{\text{total}})$ of the total field, which consisted of the incident and scattered fields, was found. Subsequently, analogous field scanning and amplitude A_{inc} and phase φ_{inc}, measurements were performed in the same region but in the absence of the scatterer, and the distribution of the complex amplitude of the incident field $P_{\text{inc}} = A_{\text{inc}} \exp(i\varphi_{\text{inc}})$ was determined. The complex amplitude of the scattered field P_{scat} was then found as the difference of the measured quantities: $P_{\text{scat}} = P_{\text{total}} - P_{\text{inc}}$. Hence, the expression for the scattered-wave amplitude $A_{\text{scat}} = \sqrt{A_{\text{total}}^2 + A_{\text{inc}}^2 - 2A_{\text{total}}A_{\text{inc}}\cos(\varphi_{\text{total}} - \varphi_{\text{inc}})}$, follows from the above, thus providing a comparison to the theory (see below). The scattered-wave phase can also be measured, but it is much more sensitive to small changes in both the positions of the measurement points and the ambient temperature than the wave amplitude. Therefore, the corresponding distributions may differ to an appreciable degree.

3.2. Theoretical Model for Investigating Acoustic Scattering by Soft Spherical Objects

As was mentioned in Introduction, the theory of acoustic scattering by a soft sphere is known well [7]. Let us present the main formulas that were used when comparing the theory to the experiment. Let a plane harmonic wave of unit amplitude propagate in the medium. Its acoustic pressure in a spherical coordinate system is expressed in the form $p_{\text{inc}} = \exp[-i(\omega t - kr\cos\theta)]$, where ω is the harmonic-wave frequency, k is the wave number, r is the distance from the origin of coordinates, and θ is the angle between the wave-propagation direction and the direction to the observation point. If the complex amplitude P_{inc} is introduced according to the formula $p_{\text{inc}} = P_{\text{inc}}\exp(-i\omega t)$, it can be represented in the form of the series

$$P_{\text{inc}} = e^{ikr\cos\theta} = \sum_{n=0}^{\infty}(2n+1)i^{-n}j_n(kr)P_n(\cos\theta), \quad (1)$$

where $j_n(kr)$ are spherical Bessel functions, and $P_n(\cos\theta)$ are nth-order Legendre polynomials. Let a spherical scatterer be positioned at the origin. The complex amplitude of a scattered wave is also expressed as an analogous series:

$$P_{\text{scat}} = \sum_{n=0}^{\infty}A_n h_n^{(1)}(kr)P_n(\cos\theta), \quad (2)$$

where $h_n^{(1)}(kr)$ are nth-order spherical Hankel functions of the first kind. In the case of a perfectly soft scatterer of radius a, the coefficients of the series are expressed as follows:

$$A_n = -\frac{(2n+1)i^{-n}j_n(ka)}{h_n^{(1)}(ka)}. \quad (3)$$

It should be noted that the approximation of a plane incident wave is poorly justified in the entire spatial region, because an actual ultrasonic beam is not only limited in the transverse direction but also has an inhomogeneous structure. At the same time, a plane wave can be reproduced with a high accuracy near a scatterer if the inhomogeneity of the ultrasound field on the scatterer scale is small. Exactly this condition was created in the above-described experiments, in which the scatterer was placed on the beam axis in the region where the wave structure was close to a plane wave. The proximity to a plane wave was checked experimentally by scanning the field in the region where the scatterer was located. Note that under these conditions, expression (1) for an incident wave is satisfied only locally, near the scatterer, but expression (2) for a scattered wave can be considered sufficiently precise globally, i.e., at large distances from the scatterer. This allows a correct comparison of the theory and experiment.

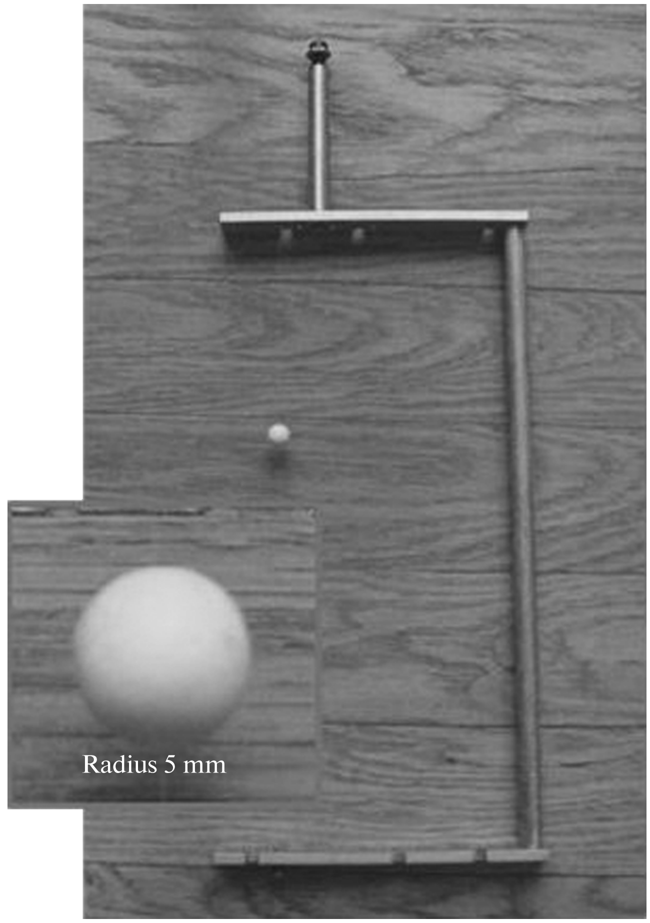

Fig. 4. Styrofoam sphere with 5-mm radius on fishing line, stretched in stiff U-shaped frame.

The complex amplitude of the scattered wave was theoretically simulated in Fortran using formulas (2) and (3). The developed program makes it possible to construct the directivity patterns of perfectly soft spherical scatterers of different radii.

3.3. Comparison of Theory and Experiment

Measurements were performed with scatterers of different size; the results show the similarity of the scattered-field structures. As an example, let us consider a scatterer with a 5-mm radius. The dependence of the pressure amplitude of the scattered wave on the distance between the center of the sphere and the scanned area on the beam axis in the forward-scattering direction was preliminarily calculated from formulas (2) and (3) (Fig. 5). The near-field zone, where oscillations occur, and the far-field zone, where the pressure slowly decreases with increasing the distance to the scatterer, can be seen. The diffraction transition from the near-field to the far-field zone is observed at

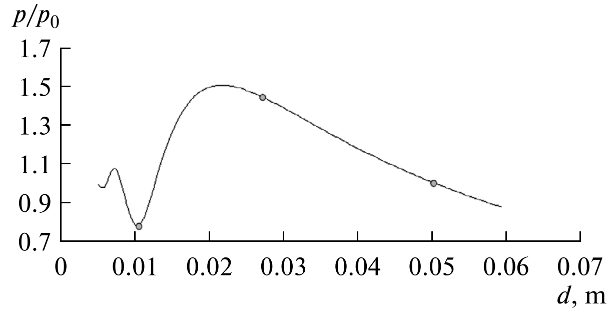

Fig. 5. Dependence of normalized amplitude of scattered-wave pressure on distance between center of sphere and scanned region. Dots denote distances at which experimental studies of scattering patterns were performed: 10, 25, and 50 mm.

a distance of 17 mm from the scatterer. On the basis of the calculated dependence, distances of greatest interest for experimental investigations of scattering patterns were chosen. The first point corresponds to the minimum of the near-field zone (10 mm), which is characterized by a "dip" at the center of the scattering pattern. The second point is the beginning of the far-field zone (25 mm), and the third is in the region of the steady-state far-field zone (50 mm).

Let us analyze the obtained transverse wave-amplitude distributions at different distances from the scatterer (Fig. 6). At a distance of $r = 10$ mm, the theory predicts a dark spot at the center (Fig. 6a), which is caused by the diffraction in the near field. Note that the experiment clearly confirms this feature of the scattered field. Moreover, the measured scattered-wave amplitude distribution at the central part of the pattern quantitatively coincides with the theoretical distribution. The only discrepancy is the presence of additional side rings in the experimental patterns. These rings weaken, as the distance r increases. The appearance of these "spurious" rings in the experiment can be explained by the influence of re-reflected acoustic waves between the scatterer and hydrophone. This artifact can hardly be avoided at short distances. This effect becomes weaker at long distances, and the experiment slightly differs from the theory. Thus, spherical styrofoam scatterers indeed properly model perfectly soft scatterers, such as gas bubbles.

4. ULTRASONIC VISUALIZATION OF SOFT SPHERICAL SCATTERERS

4.1. Schematic of Calculating the Scattering of a Pulse Signal

From the obtained results, it can be concluded that the acoustic properties of styrofoam are rather close to the acoustic properties of air, thus allowing styrofoam specimens to be used as models of gas bubbles to investigate the technique for obtaining ultrasonic images of bubbles in water or biological tissue phantoms.

In most problems of ultrasound diagnostics, pulse signals $p_{\mathrm{inc}}(t)$ are used. A typical signal has the form of a tone burst with a Gaussian envelope. Such a signal can be written as

$$p_{\mathrm{inc}}(t) = p_0 \exp\left(-t^2/\tau_0^2\right)\sin\omega_0 t. \tag{4}$$

Here, p_0 is the typical pulse amplitude, t is the time, τ_0 is the pulse duration, and ω_0 is the center cyclical frequency. To calculate the scattered field using formulas (2) and (3), an incident pulse must be represented as a Fourier integral, which is a superposition of harmonic waves, and the scattering of each spectral component must be individually considered. The resulting scattered wave at any spatial point is then a superposition of scattered waves at each frequency at this point.

In practice, instead of the Fourier integral, a finite number of terms of Fourier series are used; for this purpose, the signal periodically continues with a certain period T and the coefficients of the corresponding series are calculated:

$$P_{\mathrm{inc}}^{(m)} = \frac{1}{T}\int\limits_{-\frac{T}{2}}^{\frac{T}{2}} p_{\mathrm{inc}}(t) e^{im\frac{2\pi}{T}t}\,dt. \tag{5}$$

After substitution of (4) into (5), the following expression for the amplitudes of the harmonics is obtained in the limit of $\omega_0 T \gg 1$:

$$\begin{aligned} P_{\mathrm{inc}}^{(m)} &= \frac{p_0}{2i}\sqrt{\pi}\frac{\tau_0}{T} \\ &\times \left\{\exp\left[-\left(\frac{(\omega_m+\omega_0)\tau_0}{2}\right)^2\right]\right. \\ &\left.- \exp\left[-\left(\frac{(\omega_m-\omega_0)\tau_0}{2}\right)^2\right]\right\}, \end{aligned} \tag{6}$$

where $\omega_m = 2\pi m/T$ is the frequency of the corresponding harmonic. Incident wave (4), which represents a diagnostic ultrasonic pulse, is a superposition of plane waves at different frequencies with known amplitudes. In spherical coordinates, an incident plane wave has the form $p_{\mathrm{inc}} = \sum p_{\mathrm{inc}}^{(m)}$, where $p_{\mathrm{inc}}^{(m)} = P_{\mathrm{inc}}^{(m)} e^{-i(\omega_m t - k_m r\cos\theta)}$, $k_m = \omega_m/c$, thus, the problem reduces to the above-considered classical case of a plane harmonic wave. In this study, the described algorithm was used for theoretical analysis of diagnostic pulses scattered by soft spherical scatterers. Typical values of the parameters used in ultrasonic medical diagnostic systems were used in the calculations: pulse duration $\tau_0 = 2$ μs, center frequency $\omega_0/(2\pi) = 3$ MHz, and pulse repetition period $T = 100$ μs.

4.2. Image Construction Algorithm

To construct an ultrasonic scatterer image, a program analogous to those used in an ultrasonic scanner with an N-element transmit–receive phased array was

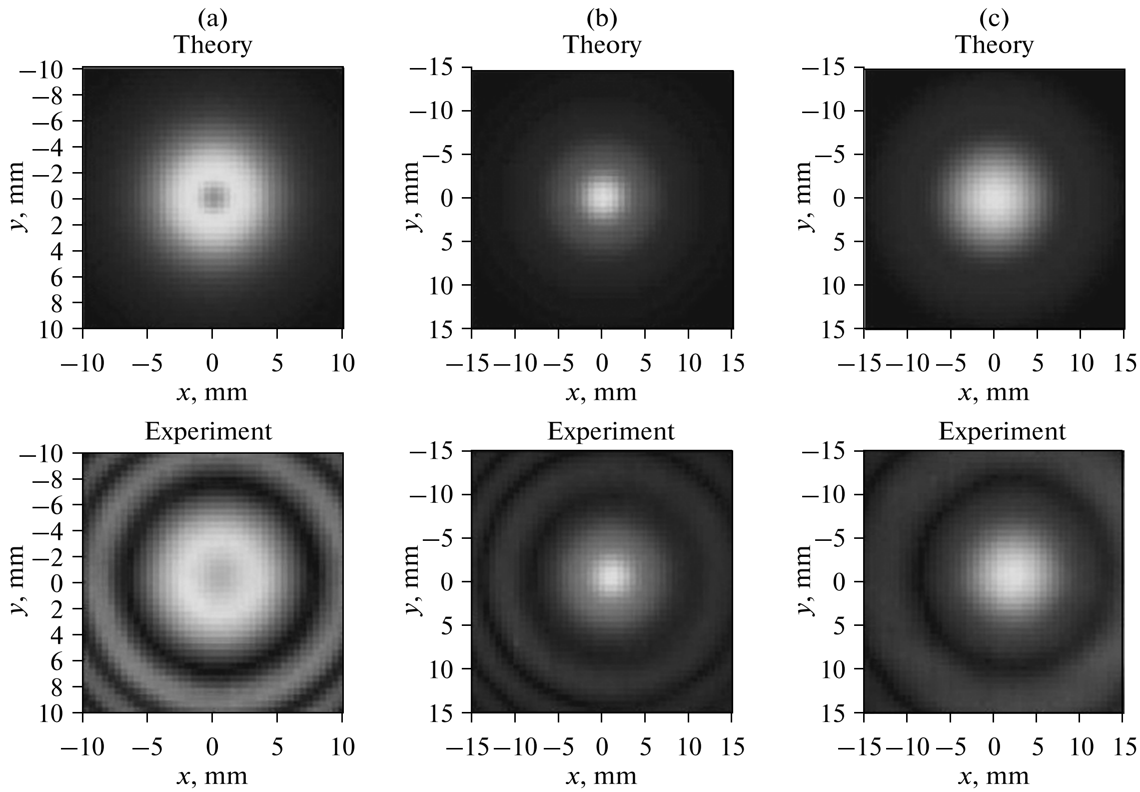

Fig. 6. Theoretical and experimental scattering patterns for soft spherical scatterer 5 mm in radius positioned at distances of (a) $d = 10$ mm, (b) 25 mm, and (c) 50 mm from center of scatterer on planes (a) 10 mm $\le x, y \le$ 10 mm; (b, c) 15 mm $\le x, y \le$ 15 mm.

developed using Matlab software. Although the developed algorithm is basically standard, it is briefly described here for clarity, because different developers of ultrasonic scanners usually add specific techniques to implement the general algorithm.

Image construction is partitioned into several stages. At the first stage, scattering signals at each of N transducers are found from the results of numerical calculation of a diagnostic pulse scattered by a soft sphere. A pulse in the form (4) was used as the incident wave. The delay is calculated for each $n = 1, \ldots, N$:

$$\tau^{(n)} = \frac{z_0 + \sqrt{z_0^2 + (x_n - x_0)^2}}{c}, \qquad (7)$$

where (x_0, z_0) are the scatterer coordinates in the visualization plane and $(x_n, 0)$ are the coordinates of the nth transducer. The first stage results in a data array in the form of a set of scattered signals that arrived at the transducers:

$$U^{(n)}(t) = U_0\left(t - \tau^{(n)}\right). \qquad (8)$$

At the next stage, the signals are digitized with a pitch of $h_t = 50$ ns; as a result, a 2D scattering data array is formed:

$$U^{(n)}(t) \to U^{(n,m)} = U^{(n)}(t = mh_t). \qquad (9)$$

To ensure extraction of the initial signal envelope, an analytical signal is introduced: $W(t) = U(t) + iV(t)$, where $U(t)$ is the initial (in-phase) signal and $V(t)$ is its quadrature component, which is related to the initial signal via the Hilbert transform. An orthogonal signal complement $V^{(n,m)}$ is found for each $U^{(n,m)}$. As a result, we have a complex array of analytical signals $W^{(n,m)} = U^{(n,m)} + iV^{(n,m)}$. The envelope is described by the magnitude of the analytical signal.

To construct an image, a mesh is introduced on the (x, z) plane with a pitch of $h = 0.5$ mm. For each point $(x_l = lh, z_k = kh)$ that is specified by a pair of indices (l, k) and for each element n of the antenna array, the delay time is found:

$$t_{lk}^{(n)} = \frac{z_k + \sqrt{z_k^2 + (x_n - x_l)^2}}{c}. \qquad (10)$$

In this time interval, the signal that reached the point (x_l, z_k) returns to the nth element. For each element from 1 to N, the value of the analytical signal $W^{(n,m)}$ at the moment $t_{lk}^{(n)}$. is found. As a rule, the value of $t_{lk}^{(n)}$ does not coincide with the values $t = mh_t$. Therefore, a linear interpolation is performed, i.e., two values of the series with the indices $\left[t_{lk}^{(n)}/h_t\right] = m_{lk}^{(n)},\ m_{lk}^{(n)} + 1$, which are nearest to $t_{lk}^{(n)}$, are determined (square brackets denote the integer part of a number) and the

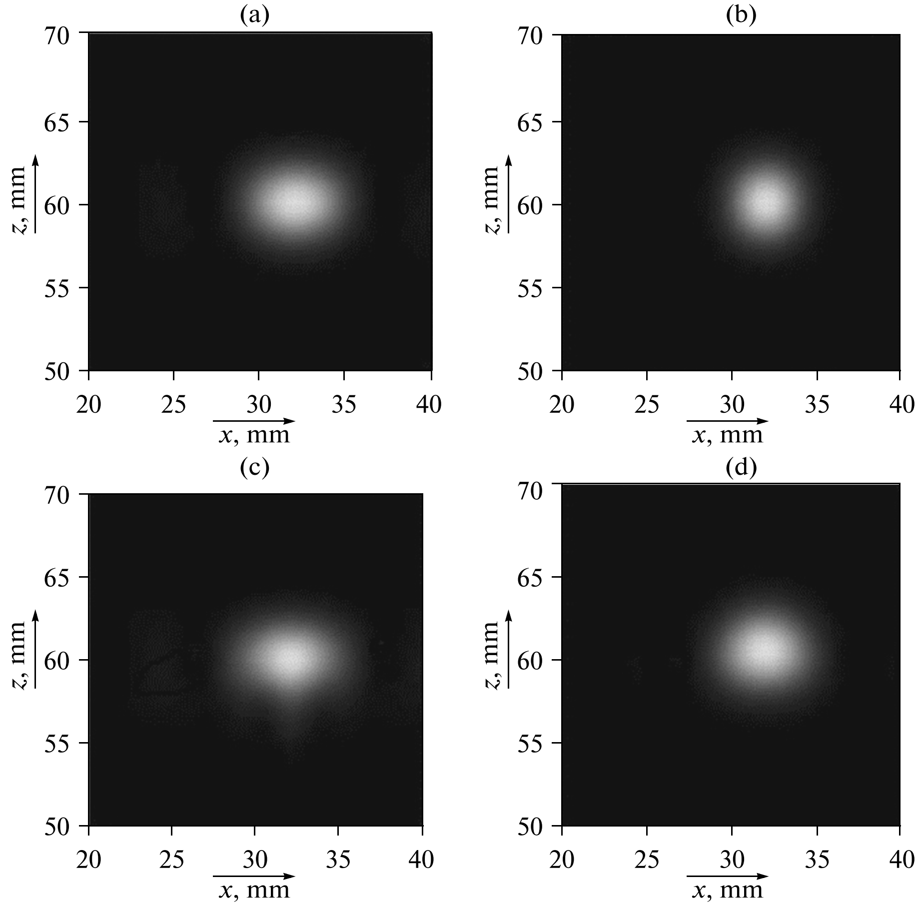

Fig. 7. Model image of point scatterer with coordinates $(x, z) = (32, 60\text{ mm})$ in mode of emission of (a) a quasi-plane wave and (b, c, d) a focused wave with focal lengths of $F = 60, 30, 90$ mm, respectively.

weighted value $F_{lk}^{(n)}$ is constructed from the values of the functions for these indices:

$$F_{lk}^{(n)} = \left(m_{lk}^{(n)} - \frac{t_{lk}{}^{(n)}}{h_t} + 1\right) W\left(n, m_{lk}^{(n)}\right) + \left(\frac{t_{lk}{}^{(n)}}{h_t} - m_{lk}^{(n)}\right) W\left(n, m_{lk}^{(n)} + 1\right). \quad (11)$$

The final stage of the algorithm is the summation of the delayed signals from all array elements and the calculation of the pattern brightness B_{lk} at a given point of the image as the square of the total magnitude of the analytical signal:

$$B_{lk} = \left|\sum_{n=1}^{N} F_{lk}{}^{(n)}\right|^2. \quad (12)$$

The described variant of image construction corresponds to emission of a plane wave by the multielement array. The situation is somewhat more complex when a transmitted wave is focused at distance F from the surface of the ultrasonic scanner. In this case, the image is constructed by sequential sending of acoustic pulses and recording of the corresponding scattered signals along each of rays 1, 2, ..., N.

The ultrasonic image of the scatterer, which was positioned at different points, was calculated by the described algorithm. As an example, Fig. 7 shows an image of a point scatterer at a point with coordinates $(x, z) = (32\text{ mm}, 60\text{ mm})$ obtained using different scanner operating modes: irradiation of the investigated region with a plane wave and a focused wave (Fig. 7). In accordance with the general features of ultrasonic image construction [11, 12], the scatterer image that was formed in the mode of irradiation with a focused wave is the most localized when the scatterer is positioned at the wave focus. If the scatterer is removed from the focus to a certain distance (nearer to or farther from the scanner) or the mode of irradiation with a plane wave is used, the scatterer image becomes blurred in the transverse direction. In any case, the size of the bright spot that corresponds to the localized scatterer is larger than the scatterer size. Hence, its size cannot be determined from the brightness pattern.

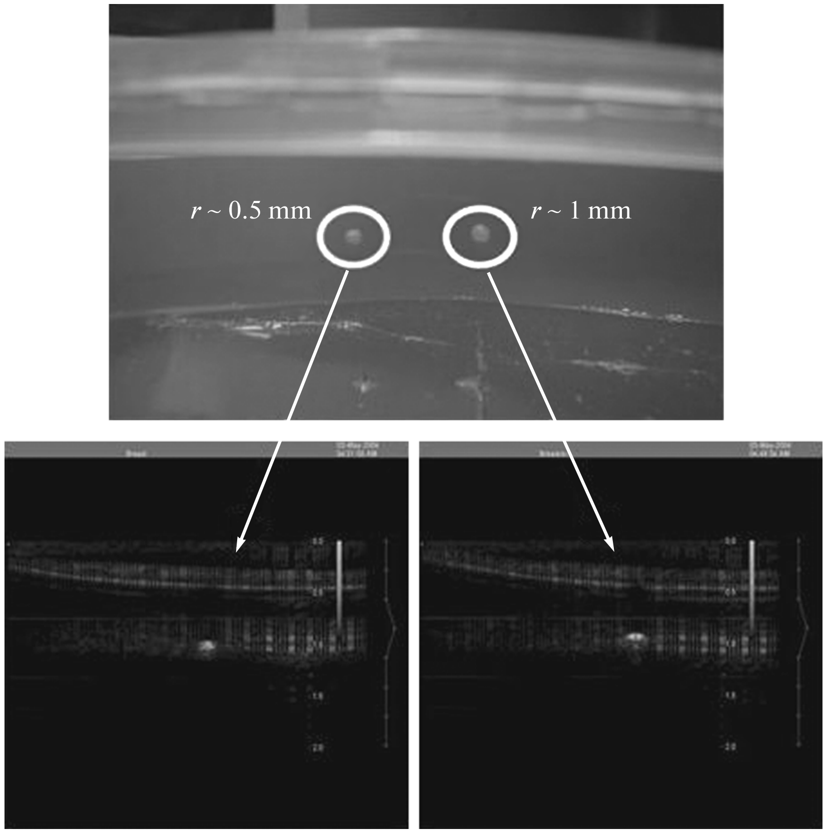

Fig. 8. Comparison of experimental images of two models of bubbles 0.5 and 1 mm in diameter.

4.3. Visualization of Spherical Styrofoam Scatterers: Technique for Measuring the True Scatterer Dimensions

A number of experiments on obtaining ultrasonic images of soft spherical scatterers were performed to compare the theoretical calculations of images of strong scatterers to observations. A Terason Ultrasound System ultrasonic scanner with a 10L5 antenna array, which consisted of 128 elements and operated at a frequency of 3 MHz, was used as the measuring instrument. An image can be observed on a computer monitor, which also includes a signal-generating unit and a data-processing unit. Gelatin was used as the investigated object (model for biological tissue), and spherical styrofoam specimens of different diameters served as strong scatterers that simulated gas bubbles.

In one of the experiments, two styrofoam specimens with diameters of 1 and 0.5 mm were taken. It was disclosed that the dimensions of the obtained ultrasonic images are virtually the same (Fig. 8); i.e., the resolution of the ultrasonic scanner did not allow us to obtain an object image with a size corresponding to the actual one: the sizes of images of both "bubbles" exceeded the true sizes.

In order to avoid the aforementioned limitation, one can use a priori information on the regularities of ultrasonic wave scattering by a perfectly soft sphere. Let us again apply the theory of sound scattering by a perfectly soft sphere and consider the scattered-signal amplitude as a function of the scatterer size. To simplify the calculations in the far-field zone ($r \to \infty$), the Hankel function asymptotics is used:

$$h_n^{(1)}(kr) \approx (-i)^{n+1} \frac{e^{ikr}}{kr}. \tag{13}$$

The formula for the scattered-field pressure at a long distance from the scatterer can be represented in the form

$$p_{\text{scat}} \approx e^{-i\omega t} f(ka, \theta) \frac{e^{ikr}}{kr}, \tag{14}$$

where

$$f(ka, \theta) = \sum_{n=0}^{\infty} (2n+1)(-i)^{2n+1} \frac{j_n(ka)}{h_n(ka)} P_n(\cos\theta). \tag{15}$$

Here, as before, a is the scatterer radius and θ is scattering angle ($\theta = 0°$ corresponds to forward scattering). From the standpoint of echo-pulse visualization, it is useful to analyze the character of changes in coefficient $f(ka, \theta)$ for different values of the scatterer radius at scattering angles $\theta = 180°$ (backscattering), 170°, 160°, and 150° (Fig. 9). Calculations show that an oscillating character of coefficient $f(ka, \theta)$ is observed in directions that form certain angles to the exact backscattering direction. In other words, when the scatterer radius or the frequency of the transmitted

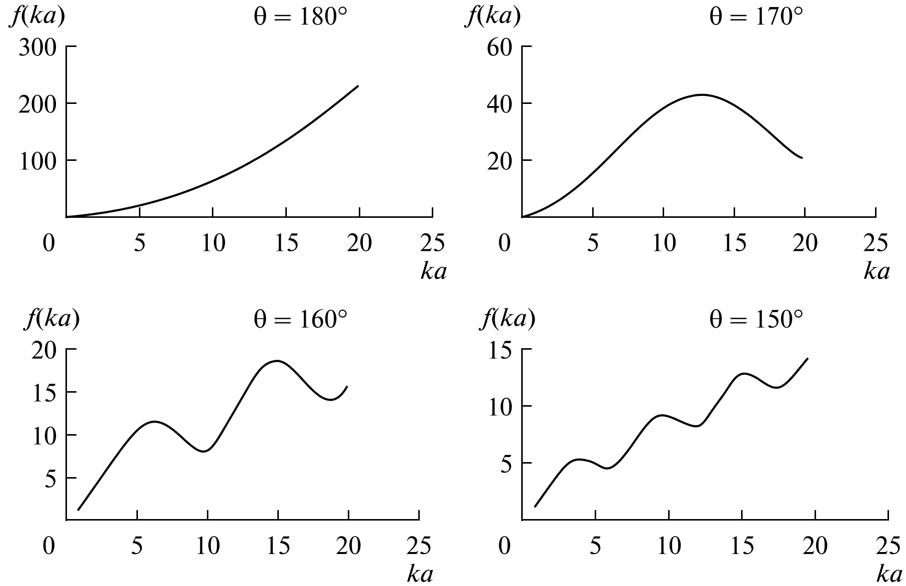

Fig. 9. Dependence of coefficient $f(ka)$ on ka at different angles θ according to formula (15).

ultrasonic signal increases, the scattered-field pressure is only a monotonically increasing function for backscattering; in other cases, it increases nonmonotonically.

The fact that the dependence of the scattering intensity on the scatterer size for backscattering is a monotonically increasing function is very important for the bubble visualization problems considered here. In fact, such a dependence makes it possible to unambiguously determine the scatterer size from the amplitude of a backscattered signal (exactly such signals are used in ultrasonic scanners for image construction). This method requires that the ultrasonic scanner be calibrated on a soft scatterer with a known size. The above-described experiments showed that styrofoam spheres can be used as standard scatterers. Subsequently, when a region with bubbles of unknown dimensions is scanned, the brightness of their images can be compared to the brightness of a standard-bubble image, and the scatterer size can be determined based on the scattered-signal level.

5. CONCLUSIONS

A model of a stationary gas bubble in water in the form of a styrofoam spherical specimen was proposed and investigated. Scattering of acoustic pulses by a perfectly soft sphere was numerically simulated. It was shown that the theoretical directivity patterns of a soft spherical scatterer virtually coincide with the experimental data for a styrofoam specimen. A program was developed that implements two operating modes of the ultrasonic scanner: with plane and focused incident waves. The calculation results obtained using this program confirmed that objects whose sizes are smaller than the instrument resolution have ultrasonic images that exceed the true size of the considered object. Experiments performed with an actual ultrasonic scanner and styrofoam models confirmed these features. The theoretical calculations for a perfectly soft sphere showed that a method for determining the true size of a scatterer from the brightness of its ultrasonic image can be achieved.

ACKNOWLEDGMENTS

This study was supported by the Russian Science Foundation, project no. 14-15-00665.

REFERENCES

1. G. S. Kino, *Acoustic Waves: Devices, Imaging and Analog Signal Analog Processing* (Prentice-Hall, 1987; Mir, Moscow, 1990).
2. C. R. Hill, J. C. Bamber, G. R. ter Haar, *Physical Principles of Medical Ultrasonics* (Wiley, 2002; Fizmatlit, Moscow, 2008).
3. M. R. Bailey, S. G. Kargl, L. A. Crum, V. A. Khokhlova, and O. A. Sapozhnikov, Acoust. Phys. **49**, 369 (2003).
4. A. Maxwell, O. A. Sapozhnikov, M. R. Bailey, L. A. Crum, Z. Xu, B. Fowlkes, Ch. Cain, and V. A. Khokhlova, Acoustics Today **8**, 24 (2012).
5. A. D. Lapin, Acoust. Phys. **44**, 364 (1998).
6. Yu. N. Makov, Acoust. Phys. **55**, 547 (2009).
7. Ph. Morse, *Vibration and Sound* (MacGraw-Hill, 1948; Gos. Izd. Tekhn.-Teor. Lit., Moscow, 1949).
8. P. Zinin, W. Weise, O. Lobkis, and S. Boseck, Wave Motion **25**, 213 (1997).
9. W. Weise, P. Zinin, A. Briggs, T. Wilson, and S. Boseck, J. Acoust. Soc. Am. **104**, 181 (1998).
10. V. E. Dontsov, V. E. Nakoryakov, and B. G. Pokusaev, Acoust. Phys. **42**, 689 (1996).
11. F. W. Kremkau, *Diagnostic Ultrasound: Principles and Instruments* (Saunders Elsevier, 2006).
12. T. L. Szabo, *Diagnostic Ultrasound Imaging* (Elsevier Academic, 2004).

Translated by A. Seferov